Journal of Sound and Vibration (2001) **246**(5), 901–926
doi:10.1006/jsvi.2001.3699, available online at http://www.idealibrary.com on IDEAL®

A MODEL FOR THE VIBRO-ACOUSTIC RESPONSE OF PLATES EXCITED BY COMPLEX FLOWS

F. HAN†

Engineering Mechanics Laboratory, General Electric Research and Development Center, One Research Circle, Niskayuna, NY 12309, *U.S.A.*

AND

L. G. MONGEAU AND R. J. BERNHARD

1077 *Ray W. Herrick Laboratories, School of Mechanical Engineering, Purdue University, West Lafayette, IN* 47907, *U.S.A.*

(*Received* 14 *March* 2000, *and in final form* 22 *March* 2001)

A model was developed and applied for predicting the vibration response of structures excited by complex vortical turbulent flows. Computational fluid dynamic (CFD) methods were utilized to model the flow over the structure. The computations allowed the general flow patterns to be identified and the mean properties of the flow field to be calculated. The spectral characteristics of the dynamic wall pressure fluctuations were obtained from an empirical database developed from genetically similar flows. The Corcos model was used to characterize the dynamic surface pressure cross-spectra. The power input into the structure was estimated accounting for the non-uniform dynamic pressure loading on the structure. The energy flow analysis (EFA) method was then used to predict the high-frequency structural vibration response and the radiated sound power. The frequency limit of the accuracy of the model was established. The model was applied to the case of a clamped rectangular homogeneous panel excited by vortical flows. The model predictions were verified experimentally for the case of an aluminium panel installed in a low-speed wind tunnel downstream of three-dimensional vortex generators. The wall pressure fluctuations, the plate transverse vibration velocity, and the acoustic pressure radiated from the plate were measured over a range of mean flow velocities. The measured surface pressure spectra beneath the coherent flow structures formed behind the vortex generators were found to be similar to those behind uniform fences at high frequencies. This confirmed that high-frequency wall pressure fluctuations depend on fine grain turbulence rather than on the large-scale flow structures. The measured panel vibration responses, and the radiated acoustic pressure levels were found to agree well with model predictions at frequencies above the model predictability threshold. The proposed modelling approach offers the opportunity to develop tools that could assist the vibro-acoustic design of complex flow-excited systems such as vehicles, or fluid machinery.

1. INTRODUCTION

Structural vibrations and noise emissions caused by flow impingement on structures occur in many practical engineering problems, in particular, vehicles and fluid machinery. These problems involve essentially the vibration of flexible structures excited by turbulent wall pressure fluctuations [1].

†The work was conducted while the first author was a Ph.D. student at the Ray W. Herrick Laboratories, Purdue University, West Lafayette, IN, U.S.A.

0022-460X/01/400901 + 26 $35.00/0

Flow-induced sound and vibration problems have been the object of many previous investigations. For example, modal analysis methods have been used to expand both the exciting wall pressure field and the radiated sound field in terms of the *in vacuo* modes of the structure for prescribed boundary conditions [2, 3]. This approach can unfortunately only be applied to a limited number of simple structures, such as simply supported plates. In most practical problems, the structures are geometrically intricate and the impinging flows complex. For example, the flow over the side-glass window of a road vehicle generally consists of vortical flows created by the A-pillar and wake flows caused by the mirror strut, as well as a fully attached boundary layer flow. The wall pressure fields under such separated and reattached flows have highly non-uniform characteristics [4]. The side-glass window itself, an irregularly shaped curved panel, is constrained by the window sealing system which must be treated as a non-uniform distributed boundary condition. Such complexity precludes the use of modal methods. Numerical methods or approximate analytical methods are needed in order to tackle this and many other analogous problems.

Statistical energy analysis (SEA) methods have been used to predict the high-frequency structural vibration response and the radiated sound power of complex flow-excited structures [5]. The use of SEA models involves the discretization of continuous systems into lumped elements. Such discretization into sub-structures does not allow the response to inhomogeneous excitations such as the dynamic surface pressures beneath complex flows to be rigorously accounted for. Wu *et al.* [6] used SEA to investigate the problem of sound radiation by a vehicle side-glass window subject to a flow excitation. The inhomogeneity of the surface pressure field was not taken into consideration. Only the reattached flow region was considered. A more sophisticated approach was followed by Strumolo [5], who considered the different flow patterns over vehicle side-glass windows. Stumolo assumed that the contribution to the total power input from each flow region was proportional to the corresponding wetted area on the window surface.

The energy flow analysis method (EFA) was developed as an alternative to SEA to predict the locally space- and frequency-averaged behavior of dynamic systems [7, 8]. Non-uniform excitations can be handled in an EFA model by using a spatially distributed power density input function. Han *et al.* [9] developed EFA models for structural vibration problems involving non-uniform flows. The wall pressure fluctuations were directly measured. The power density input was calculated in terms of the cross-power spectral density of the wall pressure field. The energy flow analysis method was used to predict the structural vibration response of a panel with non-uniform power input loading. The model was verified experimentally for a rectangular plate excited by turbulent boundary layer flows and separated–reattached flows.

The method used by Han *et al.* [9] requires *a priori* information about the wall pressure field. Such data may not be available early in the design stage of new products. The goal of this study is to extend the method of Han *et al.* [9] for cases where wall pressure fluctuations must be modelled. The ultimate goal is to develop a tool for the prediction of noise and vibration that could guide the design of complex flow-excited structural systems.

Computational fluid dynamic (CFD) models may be used to compute mean flow properties. The spectral properties of the surface pressure field can then be predicted to satisfactory accuracy, even for separated flows and reattachment flows, assuming a similarity between flows with similar gross characteristics [10]. Strumolo [5] followed this approach to predict the surface pressure spectra under different flow regions of a vehicle glass window. A CFD model of the external air flow over the vehicle was used to compute the mean flow properties. Separated vortical flow regions, reattached flow regions, and turbulent boundary layers were identified over the side-glass window panel. Using computed mean flow variables, Strumolo characterized the fluctuating pressure field over

the window using the Corcos model. Available data for surface pressure spectra under similar flow regions of a two-dimensional backward-facing step flow were used in the model. This approach was also followed considering a more detailed representation of the flow excitation and including contributions from all greenhouse surfaces (the roof and all glass panels) by Coney *et al.* [11].

Leep-Apolloni *et al.* [12] attempted a direct computation of the surface pressure spectra underneath the complex, high Reynolds number flow over a vehicle side-glass window. A commercial CFD code, PowerFlow^{TM} developed by EXA Corp., was used. The results were found to disagree with experimental data in separated flow regions. Direct numerical simulations aimed at resolving the time-varying surface pressure also require sophisticated and prohibitively expensive computations.

In this investigation, a hybrid model for predicting the vibro-acoustic response of structures under complex flow excitations is described in section 2. The proposed approach combines steady incompressible computational fluid dynamics (CFD) technique and the energy flow analysis method. The flow computations are used to obtain mean flow information. Wall pressure characteristics are obtained from the predicted mean pressure coefficient and an empirical database. The non-uniform pressure field is modelled to calculate the power density input. The energy flow analysis method is used to calculate the vibration response. In section 3, a method for calculating the frequency threshold above which the model can be considered appropriate and efficient is described. In section 4, the combined proposed model was applied to the case of a rectangular clamped plate excited by flow behind three-dimensional vortex generators. The predictions are compared with experimental results.

2. DESCRIPTION OF THE MODEL

A sketch of a typical flow-induced plate vibration and sound radiation problem is shown in Figure 1. There are four components in the problem to be modelled: (1) the dynamic wall pressure field: (2) the power density input from the flow to the plate; (3) the vibration of the plate; and (4) the sound radiation from the plate.

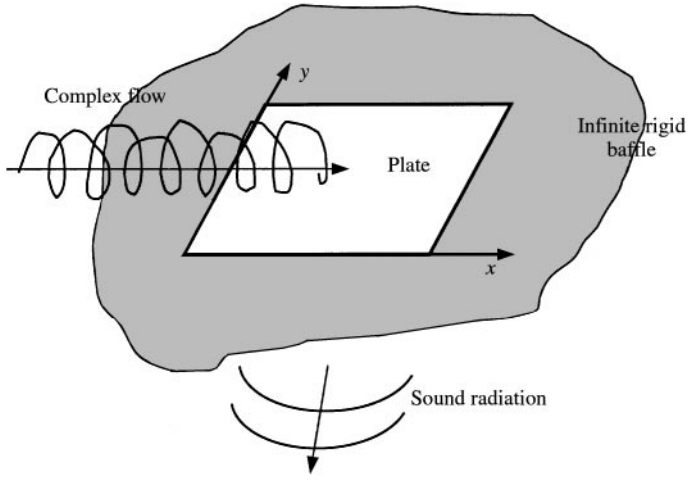

Figure 1. Sketch of a flow-induced plate vibration and sound radiation problem.

2.1. DYNAMIC WALL PRESSURE FIELD

2.1.1. *Wall pressure model*

The wall pressure field under complex flows can be approximately described using a Corcos model [5, 6, 13]. The cross-spectral density form of the Corcos model is [14, 15]

$$S_{\mathbf{x}\mathbf{x}'}(\mathbf{x}, \xi_x, \xi_y, \omega) = \Phi_{pp}(\omega, \mathbf{x}) e^{-\gamma_x|\omega\xi_x/U_c|} e^{-\gamma_y|\omega\xi_y/U_c|} e^{-j\omega\xi_x/U_c}, \quad (1)$$

where ξ_x and ξ_y is the spacing between two points $\mathbf{x}$ and $\mathbf{x}'$ along the x and y directions, respectively, γ_x and γ_y are constants related to the decay rate of the spatial coherence in the streamwise and the spanwise directions, respectively, U_c is the flow convection velocity, ω is the angular frequency, $j = \sqrt{-1}$, $\Phi_{pp}(\omega, \mathbf{x})$ is the auto-power spectral density of the wall pressure fluctuations at point $\mathbf{x}$, and $S_{\mathbf{x}\mathbf{x}'}(\xi_x, \xi_y, \omega)$ is the cross-power spectral density of wall pressure fluctuations between point $\mathbf{x} = (x, y)$ and $\mathbf{x}' = (x', y')$. The assumed time-dependence factor for this model is $e^{j\omega t}$. The flow convection velocity was assumed to be $U_c = 0{\cdot}50\ U_m$ for separated/vortex flows and $U_c = 0{\cdot}65\ U_m$ for reattached flows, where U_m is the local flow velocity. The local flow velocity is related to the free-stream flow velocity by

$$U_m = U_0\sqrt{1 - C_p}, \quad (2)$$

where C_p is the static wall pressure coefficient. Spectral quantities such as the auto-power spectral density Φ_{pp} and the coherence spectra, and mean flow properties, such as static pressure coefficient C_p, are needed in order to model the fluctuating wall pressure field.

Steady flow computations were performed to obtain the local mean flow velocity and static pressure coefficient. Spectral quantities were obtained from a database developed in the laboratory for "analogous" flows. While many researchers have conducted measurements of the surface pressure field beneath turbulent boundary layer (TBL) flows, little data are available in the literature for more complex flows. Measurements were performed to generate a database of spectral characteristics for flows behind fences and other generic vortical flows.

2.1.2. *Development of the wall pressure database*

In flow-induced structural vibration problems, frequently encountered flows include vortex flows and reattached flows [10]. A two-dimensional fence flow exhibits both these features [9]. Extensive measurements were conducted to obtain the auto-power spectral densities and coherence spectra of surface pressure fluctuations beneath flow over a fence.

The experiments were conducted in a quiet wind tunnel. The fence was installed laterally across the test section of the wind tunnel, as shown in Figure 2. The flow was primarily a two-dimensional flow, with negligible effects from the side walls of the test section. The fence was 2·3 cm high. The angle between the fence and the test section floor was 60°. The boundary layer thickness of the attached boundary layer flow far upstream the fence was 2·6 cm at a flow velocity of 31·8 m/s [16]. The ratio of the fence height and the boundary layer thickness was $h/\delta = 0{\cdot}88$. This causes large scale flow disturbances to occur. The measurements were made for flow velocities ranging from 10·0 to 40·0 m/s. The Reynolds number based on fence height ranged from $1{\cdot}58 \times 10^4$ to $6{\cdot}35 \times 10^4$.

Smoke was used to visualize the flow over the fence. The salient features of the flow over the fence are schematically illustrated in Figure 2. The flow field far upstream is an attached boundary layer flow. The flow downstream of the fence is forced to separate from the floor

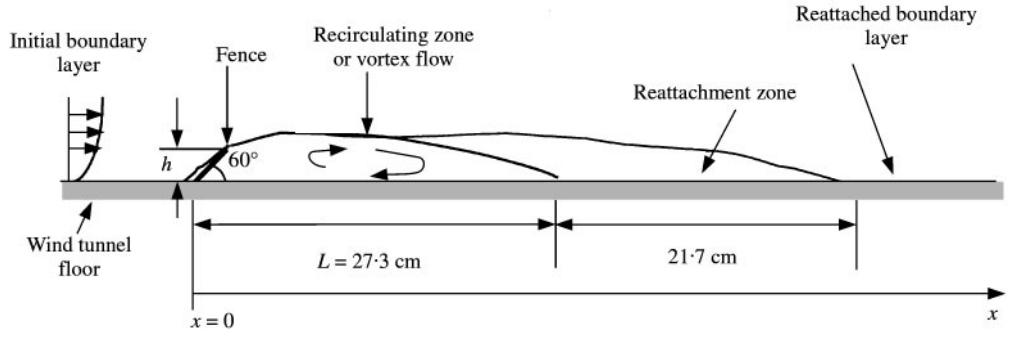

Figure 2. Sketch of the fence flow patterns ($h = 2{\cdot}3$ cm fence height, $L = 27{\cdot}3$ cm vortex size).

resulting in a free shear layer or vortex flow. It then reattaches to form an energized attached layer. This non-equilibrium attached layer undergoes a relaxation process as it is convected downstream, slowly evolving into an equilibrium boundary layer. The streamwise dimension of the vortex, L, was measured to be approximately 27·3 cm. The reattachment zone was 21·7 cm long. The size of the vortex region and that of the reattachment zone were basically independent of the flow velocity in the range between approximately 20·0 and 40·0 m/s.

Wall pressure fluctuations were sensed using a microphone array consisting of seven 0·3 cm condenser microphones mounted flush with the flat smooth test section floor. The microphone array was oriented alternately in both the streamwise and spanwise direction. The microphone separation distance was 7·00 cm. Auto-power spectral densities and cross-power spectral densities between signals from the microphones were collected using an FFT analyzer. The auto-power spectral densities were scaled using free-stream flow velocity and the vortex size in the streamwise direction. Wall pressures at the same position for different flow velocity collapsed into a single curve after being scaled. The wall pressure spectral densities measured at various positions are shown in Figure 3. At $x/L = 0{\cdot}5$, under a vortical flow, the surface pressure level is comparatively low and the energy is concentrated at very low frequencies. The maximum pressure level is found at the reattachment point ($x/L = 1{\cdot}0$). Within the reattachment zone ($1{\cdot}0 < x/L < 1{\cdot}8$) the pressure level changes only slightly. The reattachment pressures are produced by impingement of the highly turbulent vortex flow onto the floor. This flow contains low-frequency velocity fluctuations from the large-scale organized motion of the flow. As the reattached boundary layer flow is convected downstream, the low-frequency component of the pressure spectral densities decreases, as shown in the wall pressure spectral density at $x/L = 2{\cdot}9$. The flow is slowly evolving towards an equilibrium flow. Farabee and Casarella [17] observed in their step flow study that, even at a distance of 72 step heights downstream of reattachment, the wall pressure field has not recovered to produce a wall pressure spectrum characteristic of an equilibrium boundary layer. Based on the scaling dependence of the wall pressure spectra, it was found that the level of the wall pressure spectral density at a certain position is determined by the vortex size, the fluid density, the flow velocity, and the position (distance to the fence).

Coherence spectra were obtained from the cross-power spectral densities between different microphones. The decay rates, γ_x and γ_y, were obtained by regression of the exponential curve in the Corcos model. The streamwise decay constant γ_x is shown in Figure 4 as a function of position. Higher decay rates imply lower coherence. The results

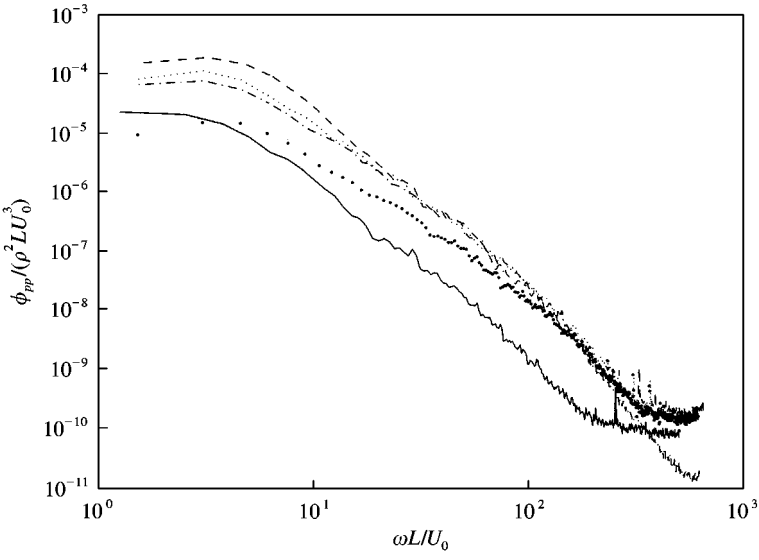

Figure 3. Wall pressure spectral densities at different positions scaled on flow velocity and vortex size: —— $x/L = 0{\cdot}5$; - - - - - $x/L = 1{\cdot}0$; -·-·-·- $x/L = 1{\cdot}8$; . . . . . $x/L = 2{\cdot}0$; ····· $x/L = 2{\cdot}9$.

shown in Figure 4 indicate that the pressure fields within the recirculating region and the reattachment zone are not as well organized as the pressure field for an attached boundary layer flow. Downstream of the reattachment, there is a coherent region of highly turbulent velocity fluctuations that is convected downstream.

In the spanwise direction, the decay rate was found to be approximately 0·58 for all cases.

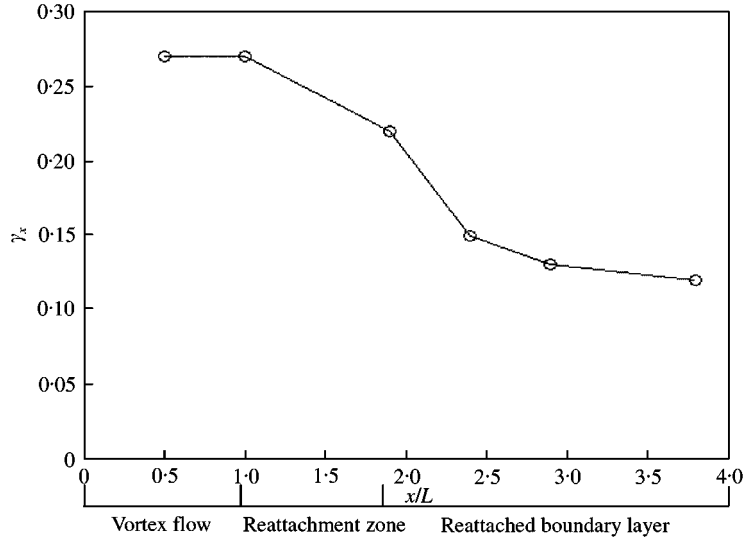

Figure 4. Measured decay rate of streamwise coherence.

2.2. POWER DENSITY INPUT

A method is needed for calculating the power density input from a non-uniformly distributed broadband loading to the structure. The distributed loading on the structure can be idealized as many discrete random forces by multiplying the pressure with an incremental area. An arbitrary number, N, of discrete, random transverse forces are assumed to be exerted on the structure. For a finite time interval $0 \leqslant t \leqslant T$, the cross-spectral density between the input force and the velocity at point i is [18]

$$S_{fv,i}(\omega, T) = \frac{1}{T} F_i(\omega, T) V_i^*(\omega, T), \tag{3}$$

where F and V represent finite Fourier transforms of the force and the transverse velocity at point i respectively. The power input to point i can be obtained from the cross-spectral density function between force and velocity, given by

$$\Pi_{in,i} = \mathrm{Re}\,[S_{fv,i}(\omega)] = \mathrm{Re}\left[\lim_{T\to\infty} \mathrm{E}\,\{S_{fv,i}(\omega, T)\}\right]. \tag{4}$$

The velocity at point i has contributions from all N forces. Therefore, V_i can be written as

$$V_i(\omega, T) = \sum_{j=1}^{N} Y_{ij}(\omega) F_j(\omega, T), \tag{5}$$

where Y_{ij} is the transfer mobility between the excitation F_j at point j and the velocity response V_i at point i. Substituting equation (5) into equation (3) and then equation (4) yields the power input at point i,

$$\Pi_{in,i}(\omega) = \sum_{j=1}^{N} \mathrm{Re}\,[S_{ij}(\omega) Y_{ij}^*(\omega)], \tag{6}$$

where S_{ij} is the cross-spectral density between forces at points i and j.

For a finite structure, the exact transfer mobility is difficult to obtain. However, the transfer mobility of an actual structure may be approximated by that of a comparable structure of infinite extent. For an infinite plate excited by two forces, the velocities at the locations of the forces can be obtained using a cylindrical travelling wave approach as [19]

$$\begin{cases} V_i = \dfrac{F_i}{8\sqrt{\rho h_s \mathbf{D}}} + \dfrac{F_j}{8\sqrt{\rho h_s \mathbf{D}}}[H_0^2(\mathbf{k}r_{ij}) - H_0^2(-\mathrm{j}\mathbf{k}r_{ij})], \\ V_j = \dfrac{F_j}{8\sqrt{\rho h_s \mathbf{D}}} + \dfrac{F_i}{8\sqrt{\rho h_s \mathbf{D}}}[H_0^2(\mathbf{k}r_{ij}) - H_0^2(-\mathrm{j}\mathbf{k}r_{ij})], \end{cases} \tag{7}$$

where $\mathbf{D}$ is the complex bending stiffness, $\mathbf{k}$ the complex wavenumber, ρ the plate density, h_s the thickness of the plate, $H_0^{(2)}$ the Hankel function of second kind, and r_{ij} is the distance between the locations of the two forces. Energy dissipation is incorporated into equation (7) by using a complex wavenumber and a complex bending stiffness.

When the loss factor is small, $\eta \ll 1$, the complex wavenumber, $\mathbf{k}$, and the complex bending stiffness, $\mathbf{D}$, can be written approximately as [20]

$$\mathbf{k} = k\left(1 - j\frac{\eta}{4}\right), \quad \mathbf{D} = D(1 + \mathrm{j}\eta), \tag{8}$$

where D is the plate bending stiffness and k is the free structural wavenumber of the plate, $k = (\rho h_s \omega^2 / D)^{1/4}$. Substituting equation (8) into equation (7), the velocities are

$$V_i = Y_{ii} F_i + Y_{ij} F_j, \qquad V_j = Y_{ji} F_i + Y_{jj} F_j, \tag{9}$$

where the transfer mobility, Y_{ij}, $i, j = 1, 2$, is

$$Y_{ij} = \frac{1}{8(D\rho h_s)^{1/2}} \left(1 - \mathrm{j}\frac{\eta}{2}\right) \left[H_0^{(2)} \left(k \left(1 + \mathrm{j}\frac{\eta}{4} \right) r_{ij} \right) - H_0^{(2)} \left(\mathrm{j}k \left(1 + \mathrm{j}\frac{\eta}{4} \right) r_{ij} \right) \right]. \tag{10}$$

The power input method developed for discrete excitation was extended to calculate the power density input from continuously distributed excitation fields. The power density input at a point was obtained by integrating the power input expression over the arbitrary excitation area. Thus, the power density input to the plate under distributed loading was expressed as

$$\pi_{in}(\mathbf{x}, \omega) = \mathrm{Re} \left[\iint_A S_{\mathbf{x}\mathbf{x}'}(\omega)\, Y^*_{\mathbf{x}\mathbf{x}'} \, \mathrm{d}\mathbf{x}' \right], \tag{11}$$

where A is the area of the structure. The transfer mobility, $Y_{\mathbf{x}\mathbf{x}'}$, is

$$Y_{\mathbf{x}\mathbf{x}'} = \frac{1}{8(D\rho h_s)^{1/2}} \left(1 - \mathrm{j}\frac{\eta}{2}\right) \left[H_0^{(2)} \left(k \left(1 + \mathrm{j}\frac{\eta}{4} \right) r \right) - H_0^{(2)} \left(\mathrm{j}k \left(1 + \mathrm{j}\frac{\eta}{4} \right) r \right) \right], \tag{12}$$

where r is the distance between the position $\mathbf{x}$ and $\mathbf{x}'$.

This method for calculating the power density input is referred to as the travelling wave method. In this method, structural wave propagation within the structure is considered. The approximation involved in this power input estimation is that the transfer mobility between an excitation point and a receiving point of a finite structure is approximated as the transfer mobility between the points of a comparable structure of infinite extent. The mobility of a finite plate varies significantly from the mobility of an infinite plate at low frequencies, and thus the use of equation (12) may cause significant errors for finite plates. However, if significant frequency- or space averaging is done, the average mobility approaches the mobility of an infinite system. At high frequencies, when the spatially averaged response is considered, this approximation was found to be reasonable.

2.3. PLATE VIBRATION RESPONSE

EFA was developed as a tool for high-frequency analysis. The governing equation for the energy density of a plate system where the vibration response can be idealized as a superposition of damped plane waves is [7]

$$-\frac{c_g^2}{\eta\omega} \nabla^2 e(x, y, \omega) + \eta\omega e(x, y, \omega) = \pi_{in}(x, y, \omega), \tag{13}$$

where e is the smooth (spatially averaged over one wavelength) and frequency-averaged energy density, and c_g is the group velocity of flexural waves in the plate. Both the power density input and the energy density are functions of position. The non-uniformity of the distributed loading and the spatial distribution of the energy density within the structure are taken into consideration.

For a rectangular plate, the EFA equation can be solved using a Fourier expansion method [7, 9]. For irregular structures, the equation can be implemented using a finite element scheme. Thus, finite element models, which are used to predict the structural response at low frequencies, can be used for high-frequency predictions as well [21].

Once the energy density of the plate is known, the vibrational velocity response can then be obtained using

$$\langle V^2(\mathbf{x})\rangle = \frac{e(\mathbf{x})}{\rho h_s}, \tag{14}$$

where V is the transverse velocity of the plate.

2.4. SOUND RADIATION

The sound power radiated from the plate into a free space was calculated using the radiation efficiency method. The radiated sound power, $\bar{P}$, is given by [20]

$$\bar{P} = \sigma \rho_0 c L_x L_y \langle \overline{V^2} \rangle, \tag{15}$$

where σ is the radiation efficiency of the plate, ρ_0 is the density of the air, c is the speed of sound in air, and the overbar denotes space averaging over the whole plate. The radiation efficiency for a rectangular plate was calculated using the approach developed by Maidanik [22].

For structures coupled with complex acoustic spaces, an energy boundary element method (EBEM) has been developed by Bitsie [23] to calculate the radiated sound power.

2.5. SUMMARY OF THE PREDICTION PROCEDURE

A hybrid prediction scheme combining CFD and EFA is proposed. The essential steps involved in the process are:

(1) Compute the external flow over a given structure using CFD. The purpose is to identify different flow regions over the structure such as the vortex flow region and reattached flow region, and to determine mean flow properties such as the static pressure coefficients in each region.
(2) Determine the wall pressure field in each flow region over the exterior surface of the structure. For vortex or reattached flow, the Corcos model is used. Mean flow properties needed in the Corcos model are obtained using the properties obtained in step 1. Spectral quantities are obtained from the database based on the results of the CFD computations and similarity arguments.
(3) Calculate the power input from the flow to the structure using the travelling wave method, equation (11).
(4) Calculate the plate vibration velocity response using the EFA equation (13).
(5) Calculate the acoustic pressure radiated from the structure using equation (15).

3. PREDICTABILITY LIMIT OF THE MODEL

In the proposed approach, the power density input from flows into the plate is calculated by assuming that the transfer mobility between two points on the plate can be

approximated by that of an infinite plate. While this is valid at high frequencies, there are significant differences between transfer mobilities of a finite structure and an infinite structure at low frequencies. The EFA method predicts frequency and space-averaged responses of structures. In the high-frequency range, EFA predictions are generally good approximations of structural responses. On the other hand, at low frequencies when the modes are separated and the modal response of the plate is important, EFA predictions are inadequate since they do not take modal responses into account. Therefore, for a particular system, it is useful and important to define a frequency threshold above which the model can be considered appropriate and efficient.

Rabbiolo [24] proposed a method to quantitatively determine the limit of predictability of a precise, deterministic approach, such as the finite element method, for the prediction of the dynamics of vibro-acoustic systems. A frequency threshold, which depends on the variability of the system, the damping factor, and the frequency bandwidth, was derived based on the modal overlap factor of the system. The value of the frequency threshold is inherent to each system. The threshold value defines a low- and a high-frequency range. In the low-frequency range, where the system response has a strong modal behavior, deterministic approaches are needed. In the high-frequency range, above the threshold, statistical methods are recommended as more appropriate and efficient.

3.1. PLATE VIBRATION

Rabbiolo's method was applied to determine the threshold frequency of the rectangular plate investigated in this study. The method is based on the calculation of the modal overlap factor. The modal overlap factor is defined as the ratio of the half-power bandwidth of a mode, $\Delta\omega$, to the average spacing between adjacent eigenfrequencies, $\delta\omega$ [24]:

$$MO(\omega) = \frac{\Delta\omega}{\delta\omega} = \frac{\eta\omega}{\delta\omega}. \tag{16}$$

The modal overlap factor can also be considered as the average number of eigenfrequencies within a half-power bandwidth. For a rectangular plate, the average frequency spacing between eigenfrequencies is [24, 25]

$$\delta\omega = \frac{8\pi k}{2A_s k - P_s}\sqrt{\frac{D}{\rho h_s}}, \tag{17}$$

where A_s is the plate surface area and $P_s = 2(L_x + L_y)$ is the plate perimeter. The modal overlap factor is thus

$$MO(\omega) = \frac{A_s k^2 \eta}{4\pi} - \frac{P_s k \eta}{8\pi}. \tag{18}$$

In practice, system responses are often averaged over an octave band or a one-third octave band to obtain frequency-averaged responses. When the frequency averaging effect on an r-fraction of a certain octave band is considered, the modal overlap factor becomes [24]

$$MO(\omega) = \frac{A_s k^2}{4\pi}\sqrt{\varepsilon^2 + \eta^2} - \frac{P_s k}{8\pi}\sqrt{\varepsilon^2 + \eta^2}, \tag{19}$$

where $\varepsilon = 2^{r/2} - 2^{-r/2}$.

As frequency increases, the number of modes contributing to the response at a given frequency becomes larger. That is, the modal overlap factor increases with frequency. Rabbiolo [24] defines the threshold or the lowest frequency of the high-frequency range of a plate as the lowest frequency at which two and a half modes participate in the response, that is,

$$MO(\omega) = 2{\cdot}5. \tag{20}$$

The frequency threshold can then be determined by solving equations (20) and (19).

3.2. SOUND RADIATION

For a rectangular plate adjacent to an acoustic free space, the spectrum of the sound radiated from the plate has fewer modal peaks than the plate vibration response below the critical frequency since only odd–odd modes are efficient in radiating sound. Odd–even and even–odd modes are less efficient and even–even modes are the least efficient in radiating sound below the critical frequency [20]. Since only one-fourth of the modes of a plate radiate, by assuming that all the modes of the plate are evenly distributed, the modal overlap factor of the sound spectrum can be considered as one-fourth of the modal overlap factor of the plate vibration below the critical frequency of the plate. That is,

$$MO(\omega) = \frac{A_s k^2}{16\pi}\sqrt{\varepsilon + \eta^2} - \frac{P_s k}{32\pi}\sqrt{\varepsilon^2 + \eta^2}. \tag{21}$$

The frequency threshold of the plate sound radiation was calculated by requiring that two and a half radiating modes participate in the acoustic response at this frequency.

Obviously, the frequency thresholds for the plate vibration and the sound radiation are different. The thresholds for the plate vibration and the sound radiation were considered as the lowest frequency of the predictability of the high-frequency model for the plate vibration and sound radiation respectively. Above the thresholds, the exact response is smoother since many modes contribute and the peaks and valleys of the modes largely cancel each other.

4. MODEL APPLICATION

There are numerous commercial CFD codes available on the market [26]. FLUENT UNS version 4.2 was used in this study. The CFD code was tested on a benchmark problem: flow over a backward-facing step. The flow through a straight channel with a sudden expansion in the lateral direction, i.e., a backward-facing step flow, was evaluated. For a backward-facing step flow, the upstream attached boundary layer separates at the edge of the step, forming a free-shear layer. The separated shear layer develops for a short distance and then impinges on the wall. The distance between the step and the attachment point is the reattachment length, x_r. The ratio of the reattachment length and the step height is the most important parameter characterizing the step flow. The result of this simulation, was compared with published experimental results [17, 27, 29–32], as shown in Table 1. The essential feature of the step flow, i.e., separation and reattachment, was captured in this CFD simulation. The reattachment length was accurately predicted. The simulation was deemed sufficiently detailed and accurate for the purposes of the current investigation.

The model was applied to a plate downstream of a pentahedral wedge vortex generator, as shown in Figure 5. The wedge was mounted on a rigid floor. The plate was

TABLE 1

Data about the backward-facing step flow

Authors	Configuration	R_h	$R_{\delta*}$	δ/h	x_r/h
This study	Small step in large channel	$2{\cdot}1 \times 10^4$			5
Farabee and Casarella [17]	Small step in large channel	$2{\cdot}3 \times 10^4$	2671	1·0	6–8
Baker [29]	Small step in large channel	5×10^4	3500	0·71	5·7–6
Abbott and Kline [30]	Sudden expansion	2×10^4–5×10^4	800–1600	0·16–1·9	6–8
Kim *et al.* [31]	Sudden expansion	$3{\cdot}0 \times 10^4$	1400	0·45	5–8
Bradshaw and Wong [32]	Sudden expansion	$4{\cdot}2 \times 10^4$	730	0·13	6

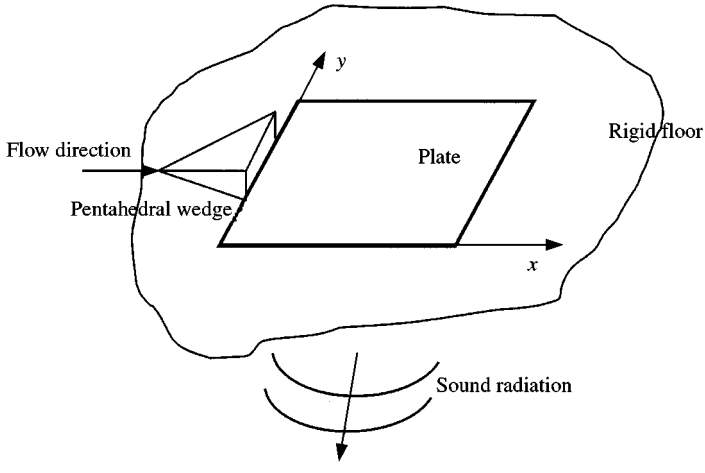

Figure 5. Sketch of the plate downstream of a pentahedral wedge.

a homogeneous rectangular panel-mounted flush with the floor. The sound from the unwetted side of the plate was assumed to radiate into a free space. The plate vibrations and sound radiated on the unwetted side were predicted following the prediction procedure listed in section 2.

Every step of the modelling process was verified using measured data. The experimental set-up is shown in Figure 6. It consisted of a rectangular steel plate which was mounted flush with the floor of a quiet flow wind tunnel test section. The plate was 47 cm long, 37 cm wide, and 0·16 cm thick. The structural damping loss factor of the plate was determined from the velocity response of the plate for an impact excitation, using the half-power bandwidth method. The results of the plate damping loss factor can be found in Han *et al.* [9]. The plate was clamped, and connected to an enclosure. Foam wedges were mounted inside the enclosure, in order to minimize sound reflections. Foam pads were installed between the test section floor and the plate to reduce the influence of the wind tunnel on the response of the plate in operation. A pentahedral wedge was mounted on the test section floor immediately upstream of the plate. The size of the pentahedral wedge is also shown in Figure 6. The boundary layer thickness of the attached boundary layer flow far upstream the fence was 2·6 cm, for a flow velocity of 31·8 m/s [16]. The ratio of the boundary layer

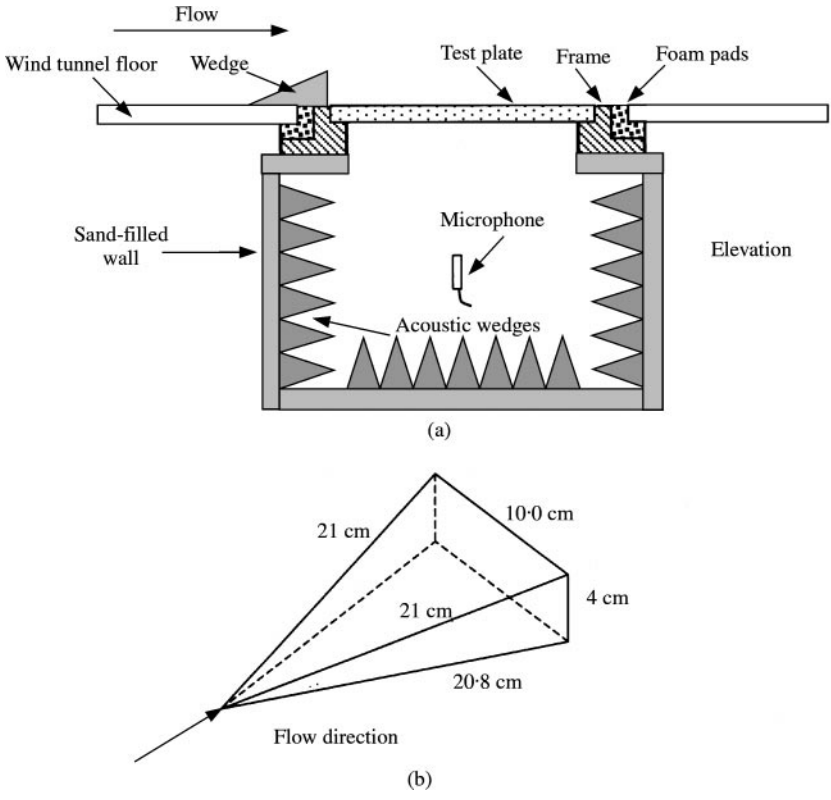

Figure 6. Sketch of (a) the plate and the anechoic enclosure, and (b) the wedge used in the experiment.

thickness and the pentahedral wedge height was 0·65. The surface pressure distribution was measured using an array of flush-mounted microphones. The transverse vibration velocity of the panel was measured using a scanning laser vibrometer. Acoustic measurements were also made in the enclosure on the quiescent side of the panel.

4.1. COMPUTED MEAN FLOW INFORMATION

For the CFD simulations, a 3-D mesh of the wind tunnel test section including the pentahedral wedge was generated using ANSYS™. The wind tunnel test section was 3·00 m long, 0·60 m wide, and 0·45 m high. A total of 7444 nodes and 16 884 triangular elements were used to develop a boundary mesh. The boundary mesh was imported into FLUENT TGID™ for automatic mesh refinement and to generate the interior mesh. There were 79 127 interior tetrahedral fluid cells. The mesh was then imported into FLUENT UNS™ for the computation. A uniform velocity profile was assumed at the inlet of the test section. The flow condition was considered incompressible and turbulent. A Reynolds stress model (RSM) was used to model the turbulent flows. The RSM is the most elaborate turbulence model available in FLUENT UNS™. It accounts for the history and transport of the Reynolds stresses in a rigorous manner. Default parameters of the RSM were used in the computation. The computation was iterated until the flow field was stable, and the computational errors were minimized.

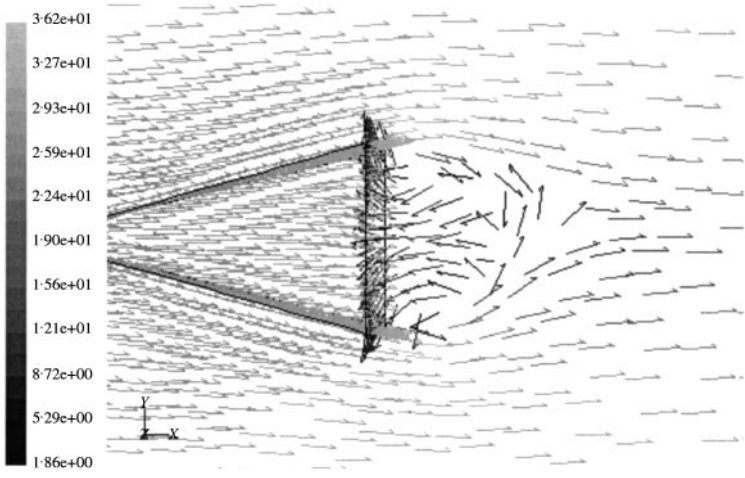

Figure 7. Velocity vector field of flow around the wedge.

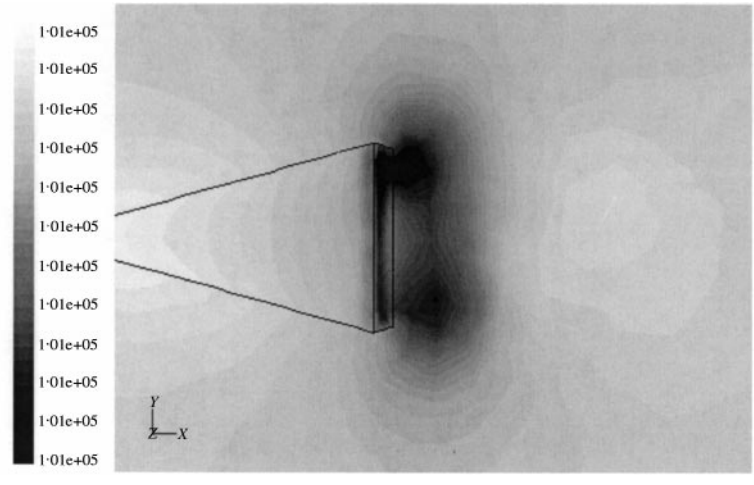

Figure 8. Static pressure distribution. The minimum pressure is 100·52 kPa; the maximum pressure is 101·86 kPa.

The predicted velocity vector field around the wedge is shown in Figure 7. The free-stream flow velocity is 30·0 m/s. Behind the wedge there is a vortex flow region. The size of the vortex in the streamwise direction is approximately 12·0 cm, which is consistent with the observations made during experiments using smoke visualization. The contour plot of the predicted static pressure on the floor and around the wedge is shown in Figure 8. Clearly, there is a low-pressure area behind the wedge, indicating that the flow there is a separated/vortex flow. The high-pressure region indicates that the flow reattaches to the floor in this area. In the study, the plate is located right behind the wedge. In general, three different flow regions are present over the plate, i.e., the separated flow, the flow reattachment and the reattached flow. This is apparent from the static pressure coefficient distribution over the plate, as shown in Figure 9.

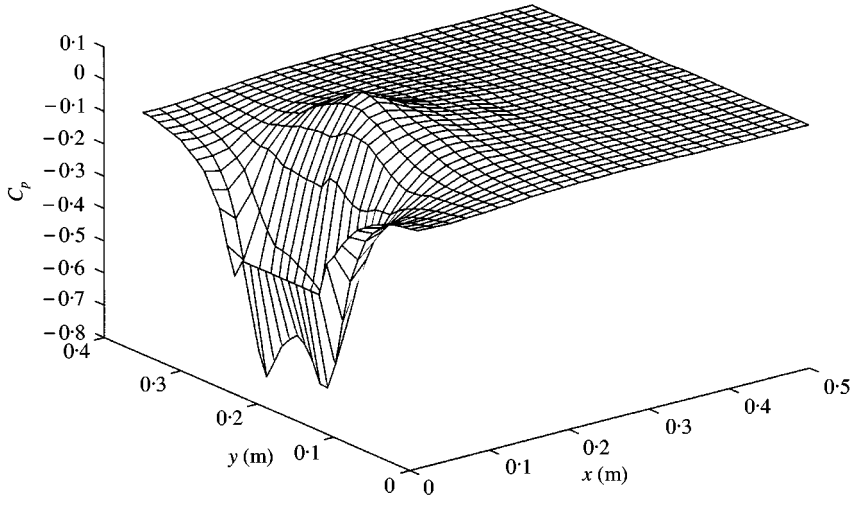

Figure 9. Static pressure coefficient distribution over the plate.

4.2. SURFACE PRESSURE CHARACTERISTICS

The next step in the prediction process is to obtain information about the spectral features of the fluctuating surface pressure field over the plate from the database based on the similarity of the fluctuating pressures for flows with similar turbulent flow structures. The spectral density level at a certain position depends on vortex size, flow velocity, fluid density, and position. Using the computed information about flow regions and vortex size, the wall pressure field over the plate was obtained from the database. In order to compare the results from the database and the measured results, two positions over the plate were chosen, as shown in Figure 10.

Point (0·120 m, 0·185 m) was investigated first. From the CFD computation, it was observed that flow reattaches to the floor at this point. Therefore, the non-dimensional

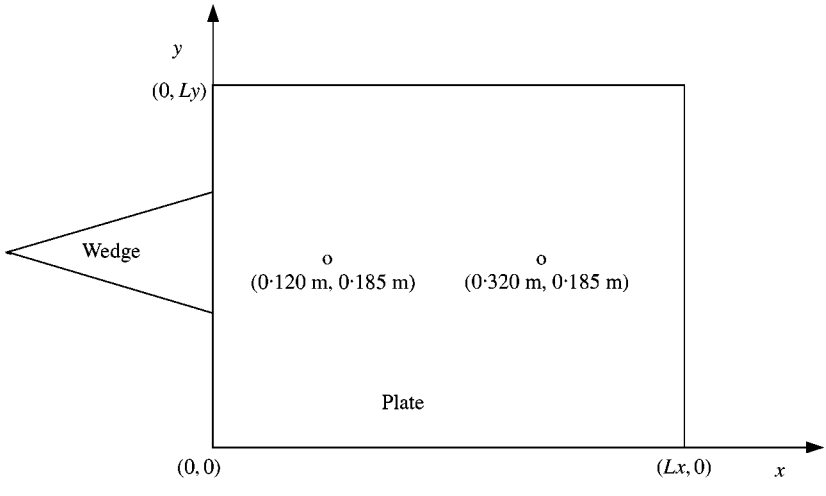

Figure 10. Positions of the two points chosen for study of the wall pressure field.

auto-power spectral density data for flow reattachment point in the database was used. Based on the computed streamwise vortex size of the wedge flow, the flow velocity, and the fluid density, the dimensional auto-power spectral density at this point was obtained. The predicted surface pressure fluctuations at this point are compared with the actual surface pressure data in Figure 11. Here the data were expressed in non-dimensional form using computed mean flow variables.

At point (0·320 m, 0·185 m), the flow is reattached. The non-dimensional auto-power spectral density data for reattached flow in the database was used. The results for position (0·320 m, 0·185 m) are shown in Figure 12.

The results obtained from the database and the measured results are generally in good agreement in the high-frequency region $\omega L/U_0 > 10$. For a flow with free-stream flow velocity of 30 m/s, the corresponding frequency region is $f > 193$ Hz. The sources of the high-frequency wall pressure fluctuations are the small-scale velocity fluctuations; the low-frequency components are caused by large-scale vortex motions of the flows. The large-scale vortical flows for the 2-D fence and the 3-D wedge have different characteristics. Therefore, at low frequencies there are significant differences between the results obtained from the database and the actual pressure fields. However, the low-frequency components are not of interest here since the prediction model is a tool only for high frequency analysis.

The decay rates of streamwise coherence obtained from the database, and those obtained from direct measurements are shown in Table 2. The results are in good agreement.

In the spanwise direction, for the two side edge regions on the plate where the effect of the wedge vortex is insignificant, an empirical wall pressure data for flat turbulent boundary layer flows was used.

4.3. POWER DENSITY INPUT

The information obtained from the simulations and the database were used in conjunction with the Corcos model to calculate the power density input from the flow to the

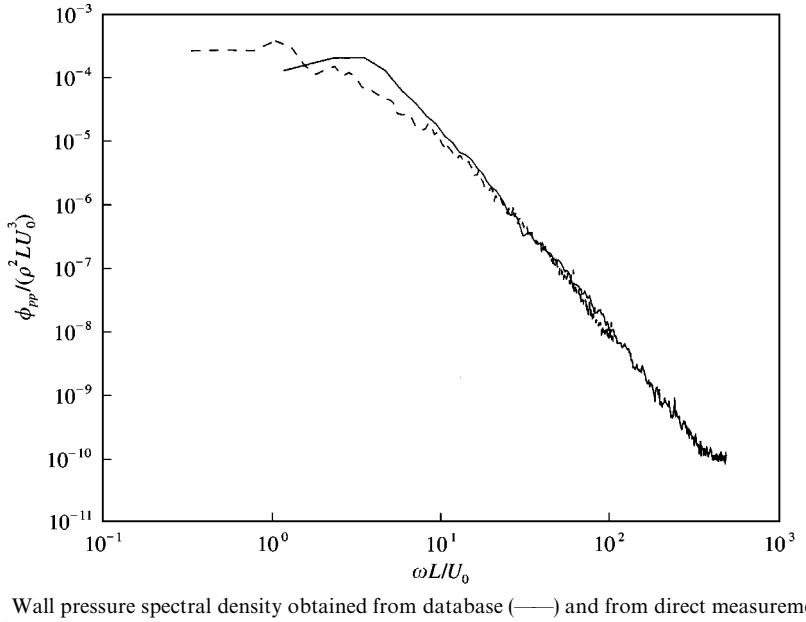

Figure 11. Wall pressure spectral density obtained from database (——) and from direct measurements (- - - - -) for position (0·120 m, 0·185 m).

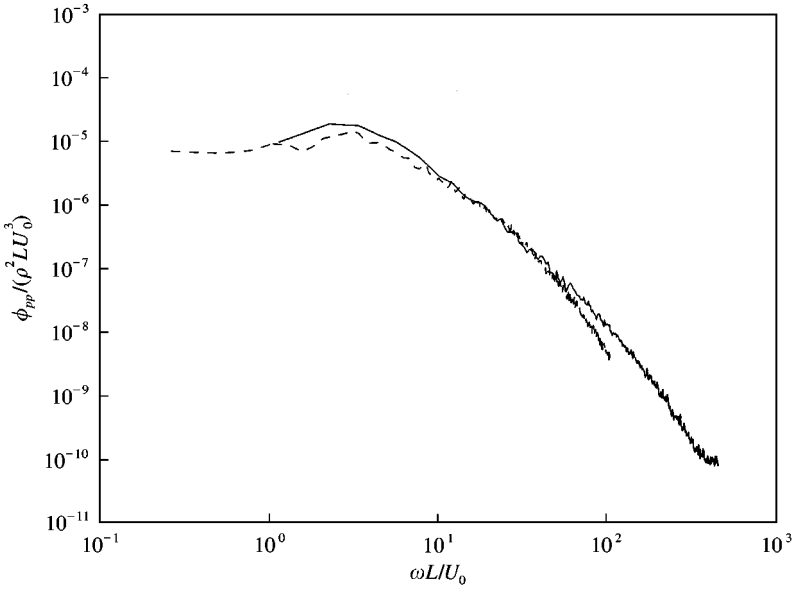

Figure 12. Wall pressure spectral density obtained from database (——) and from direct measurements (- - - - -) for position (0·32 m, 0·185 m).

TABLE 2

The decay rates of streamwise coherence at several positions for flow field around the pentahedral wedge vortex generator

Position	γ_x (database)	γ_x (measured)
(0·120 m, 0·185 m)	0·27	0·28
(0·230 m, 0·185 m)	0·22	0·16
(0·320 m, 0·185 m)	0·14	0·13
(0·420 m, 0·185 m)	0·12	0·11
(0·420 m, 0·258 m)	0·12	0·11

structure. The surface pressure field was non-uniformly distributed over the plate. Power density inputs at 15 evenly distributed grid points over the plate were calculated using the travelling wave method. The database only provides information of coherence between pressures at two adjacent positions. The decay rate of coherence between a point and distant points was assumed to be the same as that between the point and adjacent points. That is, $S_{\mathbf{x}\mathbf{x}'}$ is taken to have the pressure auto-spectrum and spatial correlation properties at $\mathbf{x}$, for all $\mathbf{x}'$. This is a reasonable assumption, since at a point far from the point of interest, the contribution to the power input is negligible due to the exponential function used in the Corcos model. The power density input distribution over the plate at 500 Hz when the free-stream flow velocity is 26·8 m/s is shown in Figure 13. The highest power input is at the reattachment point. At the reattachment point, the flow is highly turbulent and energized. As the flow is convected downstream, the turbulence intensity is decreased. The calculated power density distribution matches the distribution of the wall pressure excitation strength.

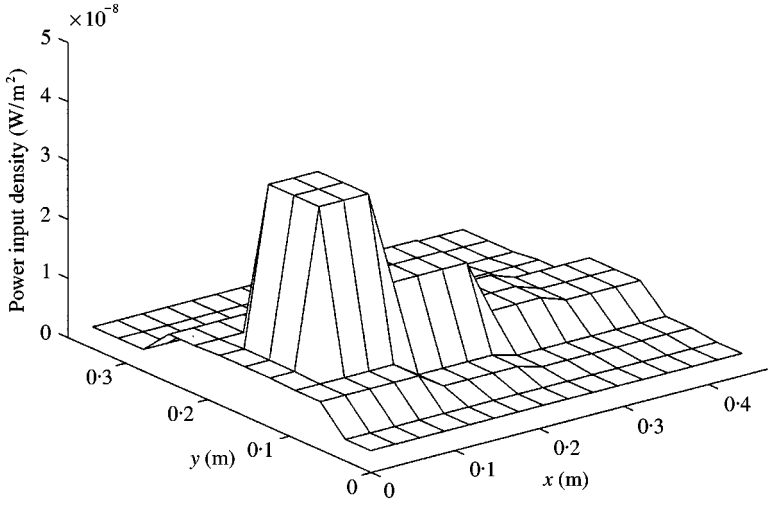

Figure 13. Power density input distribution over the plate at 500 Hz. $U_0 = 26{\cdot}8$ m/s.

4.4. VIBRATION RESPONSE OF THE PLATE

The frequency threshold of the plate was determined. When only damping is considered, the threshold of the plate was found to be 35·2 kHz. This can be considered the frequency threshold for narrowband analysis. Frequency averaging makes the responses smoother, pushing the threshold toward lower frequencies. The threshold is 355 Hz when frequency averaging over one-third octave bands is considered.

The plate vibration velocity was then obtained by solving the EFA equation, accounting for the non-uniformly distributed power input. The EFA equation was solved using the Fourier expansion technique [7, 9]. The calculated results show little spatial variation over the plate since the plate is lightly damped. The predictions are compared with the measured plate transverse velocity for a mean flow velocity of 26·8 m/s in Figure 14. Both the EFA predictions and the measured results shown here are averaged results over the whole plate surface. The measured plate vibration response exhibits strong modal behavior up to 2000 Hz, since 2000 Hz is still well below the threshold frequency for narrowband analysis.

The vibration levels in one-third octave bands are shown in Figure 15. In frequency bands below the threshold 355 Hz, there are some differences between the measured and predicted results due to the low modal density of the plate response. Above the threshold, the measured and the predicted results are in excellent agreement. The results when free-stream flow velocity is 35·8 m/s are shown in Figure 16. As before, the model works well except at very low frequencies.

4.5. SOUND RADIATION

The radiated sound power was calculated using equation (15). By assuming that the radiated acoustic pressure was uniformly distributed over a semi-spherical surface, S_s, the acoustic pressure at a single point in the enclosure below the plate was calculated simply by dividing the sound power by the surface area,

$$p^2 = \frac{\bar{P}}{\rho_0 c S_s}. \tag{22}$$

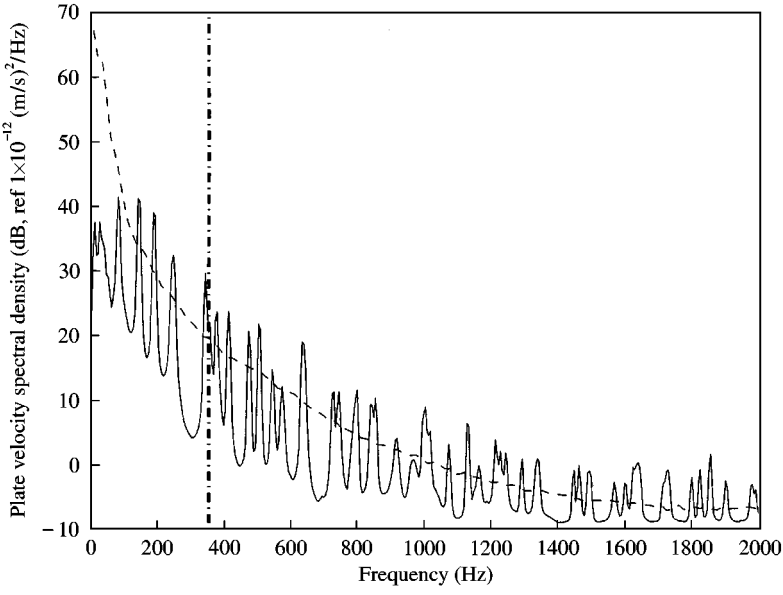

Figure 14. The space-averaged plate velocity spectral density: $U_0 = 26{\cdot}8$ m/s: —— measured; - - - - - predicted.

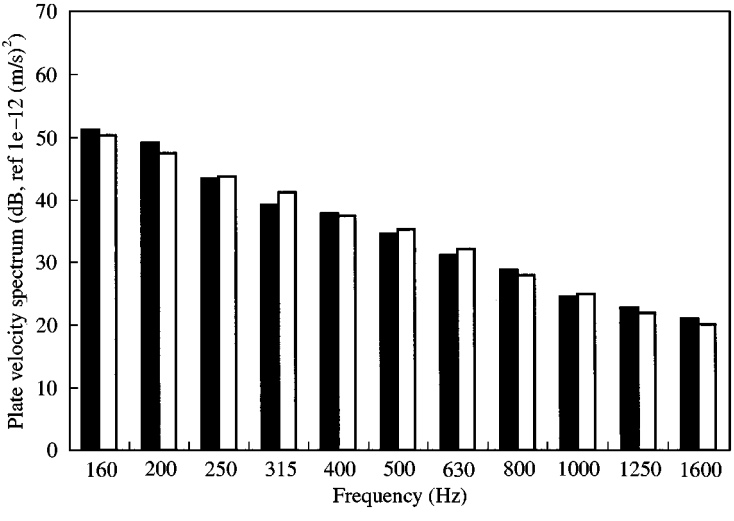

Figure 15. The space-averaged plate velocity spectra; $U_0 = 26{\cdot}8$ m/s: ■, measured; □, predicted.

The predictions, along with the measured pressures, are shown in Figure 17 for a free-stream flow velocity of 26·8 m/s. The frequency range is well below the critical frequency of the plate, which is 7·8 kHz. In this frequency range, only odd–odd modes of the plate radiate sound efficiently. Thus, the modal density of the measured pressure is very low. Equation (21) was used to calculate the frequency threshold for the radiated sound. The frequency threshold was 1305 Hz when damping and frequency averaging effects were both considered. The one-third octave band pressure levels are shown in Figures 18 and 19 for flow velocities of 26·8 m/s and 35·8 m/s respectively. Below 1305 Hz, the EFA predicts the sound level poorly. Above the threshold, in the 1600 Hz band, the prediction is in better

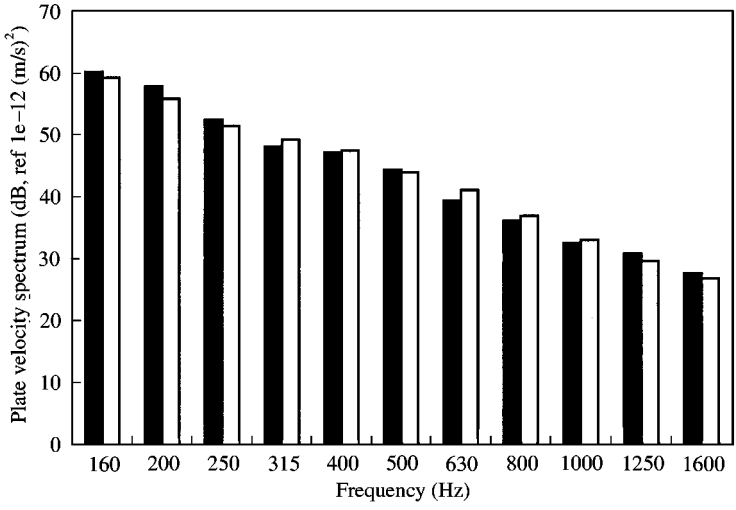

Figure 16. The space-averaged plate velocity spectra; $U_0 = 35{\cdot}8$ m/s: ■, measured; □, predicted.

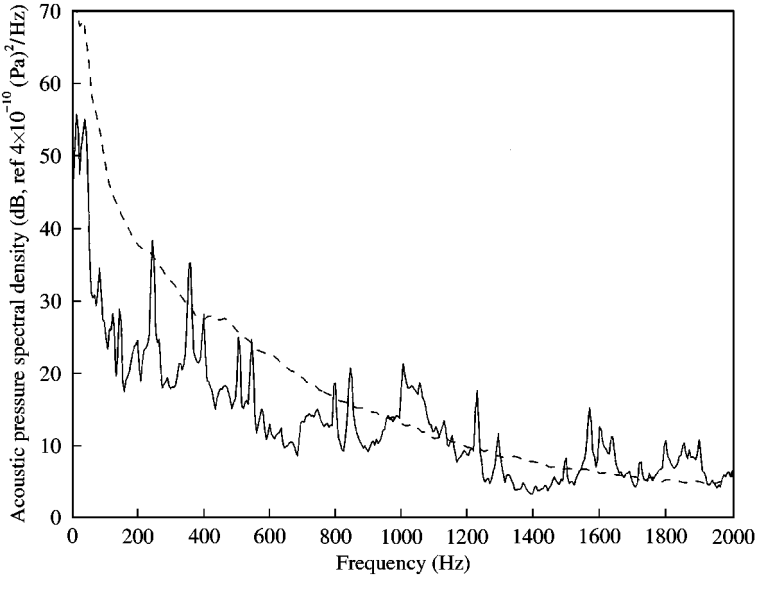

Figure 17. The acoustic pressure spectral density; $U_0 = 26{\cdot}8$ m/s: ——, measured; - - - - -, predicted.

agreement with measured sound level. Unfortunately, no data could be obtained at higher frequencies due to limitations in the sensitivity of the laser vibrometer.

5. PARAMETER AND SENSITIVITY ANALYSIS OF THE MODEL

Many parameters, such as the spectral properties of the flow field and plate properties, are specified in order to use the prediction model for any flow-induced sound and vibration problems. Some parameters such as the plate dimensions, plate material density, the fluid

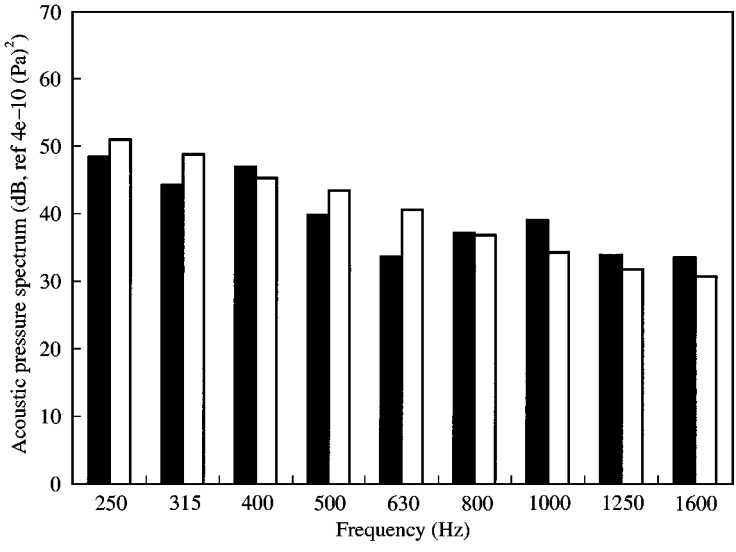

Figure 18. The acoustic pressure spectra; $U_0 = 26{\cdot}8$ m/s: ■, measured; □, predicted.

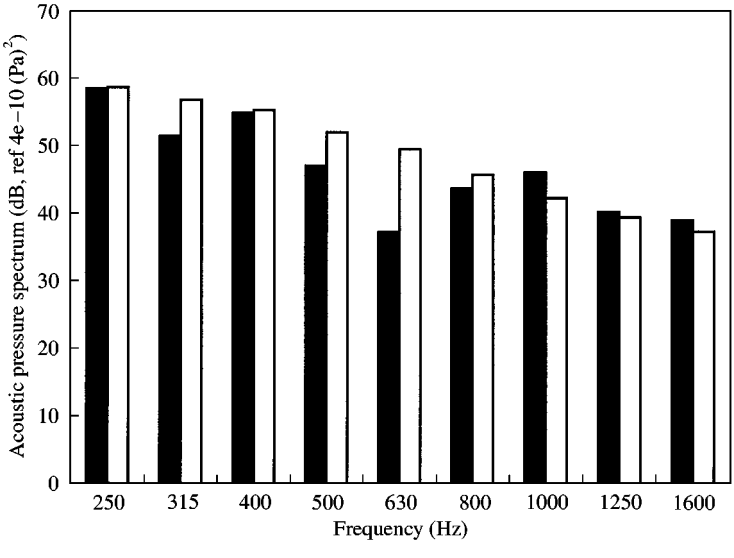

Figure 19. The acoustic pressure spectra; $U_0 = 35{\cdot}8$ m/s: ■, measured; □, predicted.

density, and the flow velocity could be easily measured or obtained from reliable sources. Others, such as the coherence decay rates and the plate damping loss factor, are either estimated empirically or indirectly measured. The influence of parameters that are directly related to the model but are hard to obtain was investigated. They include the static pressure distribution coefficient, C_p, the surface pressure auto-power spectral density, Φ_{pp}, the streamwise coherence decay rate, γ_x, the spanwise coherence decay rate, γ_y, and the plate damping loss factor, η.

The flow field parameters, i.e., C_p, Φ_{pp}, γ_x, γ_y enter the model only through the power density input formulation. The plate response does not directly depend on these flow field parameters. The plate damping loss factor directly influences both the power density input

and the vibration response of the plate. The sensitivities of the power density input to the parameters of interest mentioned above were studied. Only the sensitivity of the plate response to structural damping was evaluated.

The following definition of sensitivity is used:

$$SS = \frac{\partial \theta}{\partial \varepsilon}, \tag{23}$$

where θ is the power density input or the space-averaged plate velocity response, ε is a parameter, and SS is the sensitivity of a parameter. Due to the complexity of the relationship for the power density input the sensitivity was evaluated numerically using the approximation

$$SS \approx \frac{\theta(\varepsilon + \Delta\varepsilon) - \theta(\varepsilon)}{\Delta\varepsilon}. \tag{24}$$

The change in the power density input or the plate response was calculated for a change in a specific design parameter. The goal of the sensitivity analysis is to find the most sensitive parameter influencing the power density input and the plate vibration responses. The effect may be positive or negative, significant or negligible.

The case of the clamped plate downstream of the pentahedral wedge vortex generator for a flow velocity of 26·8 m/s was used. The five parameters mentioned above were individually increased globally in the entire frequency range by 50% each. When the sensitivity of the model to one parameter is evaluated, all the others remain unchanged. The changes in the power density input and the plate response were evaluated using $10 * \log 10\,[\theta(\varepsilon + \Delta\varepsilon)/\theta(\varepsilon)]$. The results are shown as a function of frequency for each parameter.

The results of the space-averaged power density input changes to the flow field parameters and the damping are shown in Figure 20. The most influential parameter is the auto-power spectral density of the wall pressure field. The power density input is

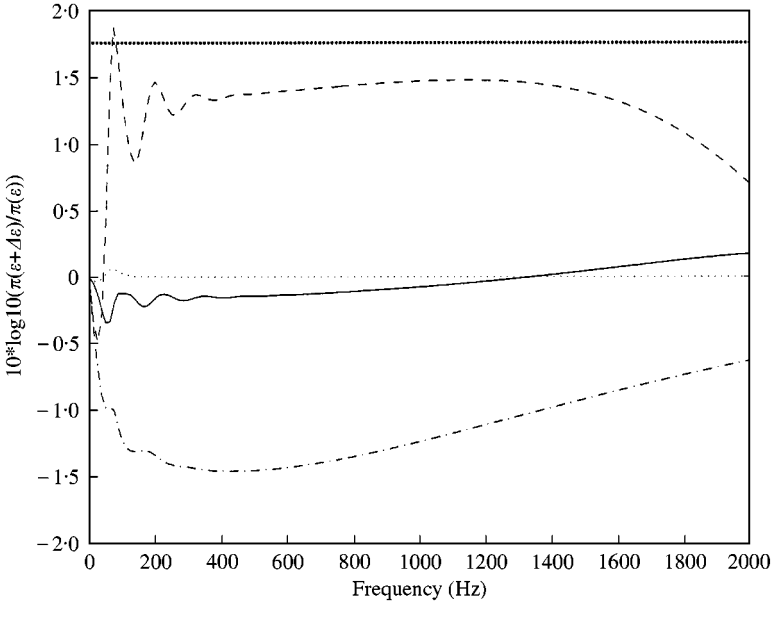

Figure 20. Power density input changes due to a change of a design parameter: ——, C_p; - - - - -, γ_x; - · - · - ·, γ_y; ……, η; ·····, Φ_{pp}.

proportional to the pressure spectral density. Therefore, a 50% increase in the pressure spectral density leads to the same amount of increase in the power density input. In general, the power density input increases with the streamwise coherence decay rate, whereas it decreases with the decay rate in the spanwise direction. The effects of each of the decay rates are important, although less significant than the auto-power spectral densities of the surface pressure fluctuations. The influence of the static pressure distribution coefficient is small. The plate damping loss factor has virtually no effect on the power density input. This is consistent with the results of an approximate analysis by Cremer and Heckl [28], in which they concluded that the power input by a harmonic point load for an arbitrary structure is independent of damping.

Due to the linear relationship between the power density input and the plate velocity responses, a change in power density input will cause the same change in the plate responses. Therefore, all of the flow field parameters have the same influence on the plate responses as on the power density input. The damping loss factor, however, enters the model not only through the power density input formulation, but also through the EFA equation. The sensitivity of the plate response to damping was also analyzed. It was found that the space-averaged plate vibration energy was reduced by a factor two across the frequency range when the damping of the plate was doubled. The change in the plate response is caused by the change of the damping value in the EFA equation. The plate response strongly depends on damping.

In summary, the auto-power spectral density of the flow field and the plate damping loss factor have a strong influence on the plate responses. The influence of the coherence decay rates is also important. The influence of the static pressure distribution coefficient on the final results is insignificant. While this sensitivity analysis does reduce the requirement on the accuracy of the static surface pressure coefficients, it still shows that an accurate CFD computation is needed to obtain the correct auto-power spectral densities of the surface pressure and reasonable estimates of the decay rates.

6. CONCLUSIONS

A model combining CFD methods, a travelling wave method for power input calculations, and EFA was proposed to predict complex flow-induced structural vibration and sound radiation responses. The prediction process involves CFD computations to identify the flow patterns over a structure and obtain mean flow information. A database of spectral information of wall pressure field under basic, commonly encountered flows was developed. Wall pressure characteristics were obtained from the database based on the results of mean flow calculation and the principle that similar flow structures have similar spectral features of pressure fluctuations. The non-uniform loading on the plate was taken into consideration using the travelling wave method to calculate the power density input. The EFA method was then used for predictions of the structural vibration, and the radiation efficiency method for radiated acoustic pressure predictions.

The model was used to study a plate excited by a flow field behind a vortex generator: a pentahedral wedge. The predictions were verified experimentally. The measured surface pressure features for different flows behind the vortex generators confirmed the model of the dynamic pressure loading on the plate. The panel vibration response and the radiated acoustic pressure levels were found to be in good agreement with the model-predicted results at frequencies where the modal overlap of the panel was sufficiently high.

A parameter and sensitivity analysis of the model was then performed. Auto-power spectral densities of the surface pressure fluctuations and the structural damping were found

to be the most influential parameters. The model was less sensitive to coherence decay rates and unaffected by the static pressure coefficient distribution.

The experimental effort of measuring surface pressure field data is unnecessary using this model. The costly requirement on computer resources and computational time for direct simulation of time-varying flow field was also avoided. All of these suggest that this prediction model is an adequate and useful tool in designing complex flow/structure systems. It can provide guidance early in the design stage.

REFERENCES

1. W. K. BLAKE 1986 *Mechanics of Flow-Induced Sound and Vibration*, Vols. I and II. New York: Academic Press.
2. W. A. STRAWDERMAN and R. S. BRAND 1968 *Journal of the Acoustical Society of America* **45**, 177–192. Turbulent flow-excited vibration of a simply supported, rectangular flat plate.
3. W. A. STRAWDERMAN and R. A. CHRISTMAN 1972 *Journal of the Acoustical Society of America* **52**, 1537–1552. Turbulence-induced plate vibrations: some effects of fluid loading on finite and infinite plates.
4. W. B. CONEY, J. Y. HER and J. A. MOORE 1997 ASME AD-Vol. 53-1, *Fluid–Structure Interaction, Aeroelasticity, Flow-Induced Vibration and Noise*, Vol. 1, 411–418. Characterization of the wind noise loading of a production automobile greenhouse surfaces.
5. G. S. STRUMOLO 1997 *Proceedings of the* 1997 *SAE Noise and Vibration Conference*, 417–423. The wind noise modeler.
6. S. F. WU *et al.* 1997 *Journal of Vibration and Acoustics* **119**, 557. Noise transmission through a vehicle side window due to turbulent boundary layer excitation.
7. O. M. BOUTHIER and R. J. BERNHARD 1995 *Journal of Sound and Vibration* **182**, 149–164. Simple models of the energetics of transversely vibrating plates.
8. Y. LASE, M. N. ICHCHOU and L. JEZEQUEL 1996 *Journal of Sound and Vibration* **192**, 281–305. Energy flow analysis of bars and beams: theoretical formulation.
9. F. HAN, R. J. BERNHARD and L. G. MONGEAU 1999 *Journal of Sound and Vibration* **227**, 685–709. Prediction of flow-induced structural vibration and sound radiation using energy flow analysis.
10. A. R. GEORGE and J. R. CALLISTER 1991 *SAE paper* 911027. Aerodynamic noise of ground vehicles.
11. W. B. CONEY, J. Y. HER and J. A. MOORE 1999 *Proceedings of the* 1999 *SAE Noise and Vibration Conference* **2**, 1237–1246. A semi-empirical approach for modeling greenhouse surface wind noise.
12. L. LEEP-APOLLONI, G. S. STRUMOLO and W. GULKER 1999 *Proceedings of the* 1999 *SAE Noise and Vibration Conference* **2**, 1231–1235. Wind noise spectral predictions using a Lattice-based method.
13. B. MASSON, P. NELSON and E. NIENALTOWSKA 1992 *DGLR/AIAA Aeroacoustic Conference, Aachen, Germany*. Development of a prediction method for the noise generated by a separated flow and transmitted by a flexible surface.
14. G. M. CORCOS 1963 *Journal of the Acoustical Society of America* **35**, 192–199. Resolution of pressure in turbulence.
15. G. M. CORCOS 1967 *Journal of Sound and Vibration* **6**, 59–70. The resolution of turbulent pressures at the wall of a boundary layer.
16. D. V. BROWN and L. MONGEAU 1995 *Ray W. Herrick Laboratories, Purdue University, Internal Report No.* 204. The design, construction, and validation of a small, low speed, quiet wind tunnel with application to noise from the flow over a cavity.
17. T. M. FARABEE and M. J. CASARELLA 1986 *Journal of Vibration, Acoustics, Stress, and Reliability in Design* **108**, 301–307. Measurements of fluctuating wall pressure for separated, reattached boundary layer flows.
18. J. S. BENDAT and A. G. PIERSOL 1986 *Random Data Analysis and Measurement Procedures*. New York: John Wiley & Sons.
19. M. C. JUNGER and D. FEIT 1986 *Sound, Structures, and their Interaction*. Cambridge, MA: The MIT Press.
20. F. FAHY 1985 *Sound and Structural Vibration: Radiation, Transmission and Response*. London: Academic Press.
21. P. E. CHO 1993 *Ph.D. Thesis, Purdue University*. Energy flow analysis of coupled structures.

22. G. MAIDANIK 1962 *Journal of the Acoustical Society of America* **34**, 809–826. Response of ribbed panels to reverberant acoustic field.
23. F. BITSIE 1996 *Ph.D. Thesis, Purdue University, West Lafayette, IN*. The structural-acoustic energy finite element method and energy boundary element method.
24. G. RABBIOLO 1998 *Herrick Lab Internal Report, HL* **98**-15. *Report* #3405-4. Definition of the limits of predictability of the dynamics of vibro-acoustic systems. Purdue University, West Lafayette, IN.
25. R. H. LYON and R. G. DEJONG 1995 *Theory and Application of Statistical Energy Analysis*. London: Butterworth-Heinemann.
26. C. J. FREITAS 1995 *Journal of Fluids Engineering* **117**, 208–218. Perspective: selected benchmarks from commercial CFD codes.
27. J. K. EATON and I. P. JOHNSTON 1982 *American Institute of Aeronautics and Astronautics* **19**, 1093–1100. A review of research on subsonic turbulent flow reattachment.
28. L. CREMER and M. HECKL 1988 *Structure-Borne Sound*. New York: Springer-Verlag.
29. S. BAKER 1977 *Ph.D. thesis, Department of Civil Engineering, University of Surrey*. Regions of recirculating flow associated with two-dimensional steps.
30. D. E. ABBOTT and S. J. KLINE 1962 *Journal of Basic Engineering* **84D**, 317–325. Experimental investigation of subsonic turbulent flow over single and double backward-facing steps.
31. J. KIM et al. 1978 *Department of Mechanical Engineering, Stanford University, Rept. MD*-37. Investigation of separation and reattachment of a turbulent shear layer: flow over a backward-facing step.
32. P. BRADSHAW and F. Y. F. WONG 1972 *Journal of Fluid Mechanics* **52**, 113–135. The reattachment and relaxation of a turbulent shear layer.

APPENDIX A: NOMENCLATURE

A_s	plate surface area
c	speed of sound
c_g	wave group speed
D	bending stiffness
e	energy density
E	Young's modulus
$\mathbf{E}$	complex Young's modulus
F	force Fourier coefficient
h	fence height
h_s	plate thickness
$H_0^{(2)}$	Hankel function of second kind
k	structural free wavenumber
$\mathbf{k}$	complex structural wavenumber
k_x	streamwise wavenumber
k_y	spanwise wavenumber
L	dimension of vortex
L_x	length of plates
L_y	width of plates
P_s	plate perimeter
P	sound power
S	cross-power spectral density of wall pressure field
t	time
T	time period
U_0	free-stream flow velocity
U_c	convection velocity of turbulence
U_m	local flow velocity
V	structural transverse vibration velocity
x	X co-ordinate
y	Y co-ordinate
$\mathbf{x}$	$\mathbf{x} = (x, y)$
$\mathbf{y}$	$\mathbf{y} = (x, y)$
Y	transfer mobility

Φ_{pp}	auto-power spectral density
γ_x	decay rate of streamwise coherence
γ_y	decay rate of spanwise coherence
η	structural damping loss factor
π_{in}	power density input
Π_{in}	power input
ρ	density of plates
ρ_0	density of fluid
σ	radiation efficiency
ω	angular frequency
ξ_x	streamwise distance
ξ_y	spanwise distance